

# Avionics-Based GNSS Integrity Augmentation for Unmanned Aerial Systems Sense-and-Avoid

Roberto Sabatini, *RMIT University – School of Aerospace, Mechanical and Manufacturing Engineering (Australia)*

Terry Moore, *University of Nottingham – Nottingham Geospatial Institute (UK)*

Chris Hill, *University of Nottingham – Nottingham Geospatial Institute (UK)*

## BIOGRAPHIES

Associate Professor Roberto Sabatini has 25 years of professional experience in the aviation industry and in academia. He is an expert in Research, Development, Test and Evaluation (RDT&E) of Avionics and Air Traffic Management Systems (ATM), with specific hands-on competence in Air Navigation Safety and Integrity, Systems for Green Operations, Aviation Human Factors Engineering, and Multi-Sensor Data Fusion.

Professor Terry Moore is the Director of the Nottingham Geospatial Institute. He was promoted to the UK's first Chair of Satellite Navigation in 2001 and has extensive research experience in a range of subjects including satellite navigation and positioning, geodesy and orbit determination. He is the founding Director of GRACE, the GNSS Research and Applications Centre of Excellence, which is jointly funded by the University of Nottingham and East Midlands Development Agency. Professor Moore is a Fellow of the Institute of Navigation and of the Royal Institute of Navigation.

Doctor Chris Hill is Principal Research Officer in the Nottingham Geospatial Institute. He has extensive R&D experience in GNSS, Differential GNSS and Integrated Navigation Systems for land, marine and aeronautical applications.

## ABSTRACT

This paper investigates the synergies between a GNSS Avionics Based Integrity Augmentation (ABIA) system and a novel Unmanned Aerial System (UAS) Sense-and-Avoid (SAA) architecture for cooperative and non-cooperative scenarios. The integration of ABIA with SAA has the potential to provide an integrity-augmented SAA solution that will allow the safe and unrestricted access of UAS to commercial airspace. The candidate SAA system uses Forward-Looking Sensors (FLS) for the non-cooperative case and Automatic Dependent Surveillance-Broadcast (ADS-B) for the cooperative case. In the non-cooperative scenario, the system employs navigation-based image stabilization with image morphology operations and a multi-branch Viterbi filter for obstacle detection, which

allows heading estimation. It utilizes a Track-to-Track ( $T^3$ ) algorithm for data fusion that allows combining data from different tracks obtained with FLS and/or ADS-B depending on the scenario. Successively, it utilizes an Interacting Multiple Model (IMM) algorithm to estimate the state vector allowing a prediction of the intruder trajectory over a specified time horizon. Both in the cooperative and non-cooperative cases, the risk of collision is evaluated by setting a threshold on the Probability Density Function (PDF) of a Near Mid-Air Collision (NMAC) event over the separation area. So, if the specified threshold is exceeded, an avoidance manoeuvre is performed based on a heading-based Differential Geometry (DG) algorithm and optimized utilizing a cost function with minimum time constraints and fuel penalty. In addition, the optimised avoidance trajectory considers the constraints imposed by the ABIA in terms of GNSS constellation satellite elevation angles, preventing degradation or losses of navigation data during the whole SAA loop. This integration scheme allows real-time trajectory corrections to re-establish the Required Navigation Performance (RNP) when actual GNSS accuracy degradations and/or data losses take place (e.g., due to aircraft-satellite relative geometry, GNSS receiver tracking, interference, jamming or other external factors). Various simulation case studies were accomplished to evaluate the performance of the Integrity-Augmented SAA (IAS) architecture. The selected host platform is the AEROSONDE Unmanned Aerial Vehicle (UAV) and the simulation cases address a variety of cooperative and non-cooperative scenarios in a representative cross-section of the AEROSONDE operational flight envelope. The simulation results show that the IAS architecture is an excellent candidate to perform high-integrity Collision Detection and Resolution (CD&R) utilizing GNSS as the primary means of navigation, providing solid foundation for future research and developments in this domain.

## 1. INTRODUCTION

In addition to Space Based Augmentation Systems (SBAS) and Ground Based Augmentation Systems (GBAS), Global Navigation Satellite System (GNSS) augmentation can also take the form of additional information being provided by other avionics systems.

In most cases, the additional avionics systems operate via separate principles than the GNSS and, therefore, are not subject to the same sources of error or interference. A system such as this is referred to as an Avionics-Based or Aircraft-Based Augmentation System (ABAS). GBAS and SBAS address all four cornerstones of GNSS performance augmentation, namely: accuracy, integrity, availability and continuity. The ABAS approach is particularly well suited to increase the levels of integrity and accuracy (as well as continuity in multi-sensor data fusion architectures) of GNSS in a variety of mission- and safety-critical aviation applications. In Unmanned Aerial System (UAS) applications, airworthiness requirements for both cooperative and non-cooperative Sense-and-Avoid (SAA) impose stringent GNSS data integrity requirements. Therefore, a properly designed and certifiable Avionics Based Integrity Augmentation (ABIA) capability would allow an extended spectrum of autonomous and safety-critical operations by continuously monitoring GNSS integrity levels and providing suitable caution and warning signals to the remote pilot or to the avionics flight control systems in order to accomplish GNSS-based mission and safety-critical tasks. This increased level of integrity could provide a pathway to support the unrestricted access of UAS to commercial airspace. Although current and likely future SBAS/GBAS augmentation systems can provide significant improvement of GNSS navigation performance, a properly designed and flight certified ABAS/ABIA system could play a key role in GNSS integrity augmentation for aviation safety-critical applications, including UAS SAA. Furthermore, using suitable data link and data processing technologies on the ground, a certified ABAS capability could be a core element of a future GNSS Space-Ground-Avionics Augmentation Network (SGAAN).

## 2. ABIA SYSTEM RESEARCH

Previous research on ABIA systems demonstrated the potential of this technology to enhance GNSS integrity performance in a variety of mission- and safety-critical applications including experimental flight test/flight inspection, precision approach and automatic landing [1-5]. Therefore, an advanced ABIA system was developed for UAS applications (Fig. 1). In this system, the on-board sensors provide information on the aircraft relevant flight parameters (navigation data, engine settings, etc.) to an Integrity Flag Generator (IFG), which is also connected to the GNSS system. Using the available data on GNSS and the relevant aircraft flight parameters, integrity signals are generated which can be sent to the UAV Ground Control Station (GCS) or used by a Flight Path Optimisation Module (FPOM). This system addresses both the predictive and reactive nature of GNSS integrity augmentation by producing suitable integrity flags (cautions and warnings) in case of predicted/ascertained GNSS data losses or unacceptable signal degradations exceeding the Required Navigation Performance (RNP) specified

for each phase of flight, and providing guidance information to the remote pilot/autopilot to avoid further data losses/degradations.

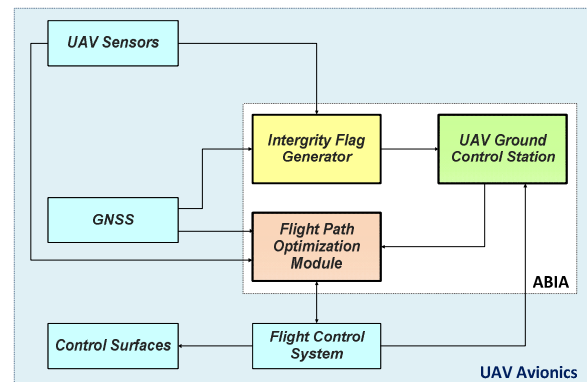


Fig. 1. ABIA system architecture for UAS applications.

To achieve this, the Integrity Flag Generator (IFG) module produces the following integrity flags [1-3]:

- **Caution Integrity Flag (CIF):** a predictive announcement that the GNSS data delivered to the avionics system is going to exceed the RNP thresholds specified for the current and planned flight operational tasks (GNSS alert status).
- **Warning Integrity Flag (WIF):** a reactive announcement that the GNSS data delivered to the avionics system has exceeded the RNP thresholds specified for the current flight operational task (GNSS fault status).

The following definitions of Time-to-Alert (TTA) are applicable to the ABIA system [1-3]:

- **ABIA Time-to-Caution (TTC):** the minimum time allowed for the caution flag to be provided to the user before the onset of a GNSS fault resulting in an unsafe condition.
- **ABIA Time-to-Warning (TTW):** the maximum time allowed from the moment a GNSS fault resulting in an unsafe condition is detected to the moment that the ABIA system provides a warning flag to the user.

### 2.1 ABIA Integrity Flag Generator

The main causes of GNSS data degradation or signal losses in aviation applications were deeply analysed in [1] and are listed below:

- Antenna obscuration (i.e., obstructions from the wings, fuselage or empennage during maneuvers);
- Adverse satellite geometry, resulting in high Position Dilution of Precision (PDOP);
- Fading, resulting in reduced carrier to noise ratios ( $C/N_0$ );
- Doppler shift, impacting signal tracking and acquisition/reacquisition time;

- Multipath effects, leading to a reduced  $C/N_0$  and to range/phase errors;
- Interference and jamming.

Understanding the physics of these phenomena and developing reliable mathematical models was essential in order to properly design the ABIA IFG module [1]. Fig. 2 shows the architecture of the IFG module and its interfaces.

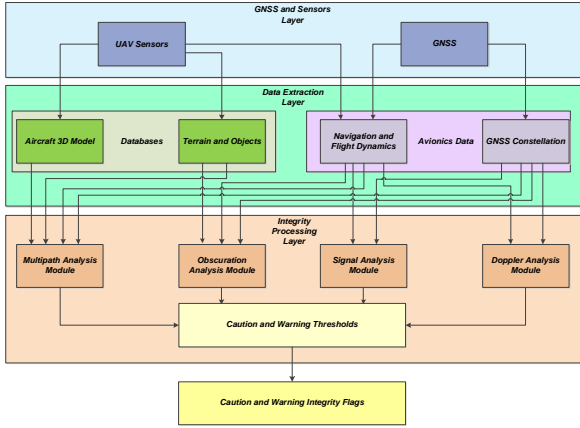


Fig. 2. ABIA IFG module architecture.

The ABIA IFG module is designed to provide CIF and WIF alerts in real-time (i.e., in accordance with the specified TTC and TTW requirements in all relevant flight phases). IFG module inputs are from the GNSS receiver and other aircraft sensors. The GNSS and Sensors Layer (GSL) passes the aircraft Position, Velocity, Time (PVT) and attitude (Euler angles) data (from the on board Inertial Navigation Systems, Air Data Computer, etc.), GNSS data (raw measurements and PVT) and the Flight Control System (FCS) actuators data to the Data Extraction Layer (DEL). At this stage, the required Navigation and Flight Dynamics (NFD) and GNSS Constellation Data (GCD) are extracted, together with the relevant information from an aircraft Three-Dimensional Model (3DM) and from a Terrain and Objects Database (TOD). The 3DM database is a detailed geometric model of the aircraft built in a Computer Aided Three-dimensional Interactive Application (CATIA). The TOD uses a Digital Terrain Elevation Database (DTED) and additional man-made objects data to obtain a detailed map of the surfaces neighbouring the aircraft. In the Integrity Processing Layer (IPL), the Doppler Analysis Module (DAM) calculates the Doppler shift by processing the NFD and GCD inputs. The Multipath Analysis Module (MAM) processes the 3DM, TOD, GNSS Constellation Module (GCM) and A/C Navigation/Dynamics Module (ADM) inputs to determine multipath contributions from the aircraft (wings/fuselage) and from the terrain/objects close to the aircraft. The Obscuration Analysis Module (OAM) receives inputs from the 3DM, GCS and ADS, and computes the GNSS antenna obscuration matrices corresponding to the various aircraft manoeuvres. The Signal Analysis Module (SAM) calculates the link

budget of the direct GNSS signals received by the aircraft in the presence of atmospheric propagation disturbances ( $C/N_0$ ), as well as the applicable radio frequency interference and Jamming-to-Signal ratio (J/S) levels. The Integrity Flags Layer (IFL) uses a set of predefined CIF/WIF threshold parameters to trigger the generation of both caution and warning flags associated with antenna obscuration, Doppler shift, multipath, carrier, interference and satellite geometry degradations. The approach adopted to set-up thresholds for the ABIA CIF and WIF integrity flags is depicted in Fig. 3.

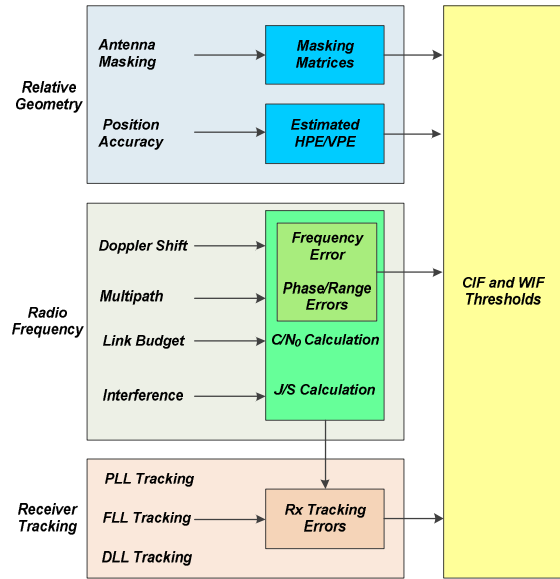


Fig. 3. Integrity flag thresholds.

The masking integrity flag criteria are the following:

- When the current aircraft manoeuvre will lead to less than 4 satellites in view, the CIF shall be generated.
- When less than 4 satellites are in view, the WIF shall be generated.

Additionally, when only four satellites are in view:

- When one (or more) satellite(s) elevation angle (antenna frame) is less than 10 degrees, the caution integrity flag shall be generated.
- When one (or more) satellite(s) elevation angle is less than 5 degrees, the warning integrity flag shall be generated.

From the definition of Dilution of Precision (DOP) factors, GNSS accuracy can be expressed by [6]:

$$\sigma_p = \text{DOP} \times \sigma_{\text{URE}} \quad (1)$$

where  $\sigma_p$  is the standard deviation of the positioning accuracy and  $\sigma_{\text{URE}}$  is the standard deviation of the satellite pseudorange measurement error. For the C/A-code  $\sigma_{\text{URE}}$  is in the order of 33.3m. Therefore, the 1-sigma Estimated Position, Horizontal and Vertical Errors of a GNSS receiver can be calculated using the PDOP (EPE in 3D), the HDOP (EHE in 2D) or the

VDOP (EVE). In order to generate CIFs and WIFs that are consistent with current GNSS RNP, we need to introduce the Horizontal and Vertical Accuracy (HA/VA) requirements in the various flight phases. The Horizontal Alert Limit (HAL) is the radius of a circle in the horizontal plane, with its centre being at the true position, which describes the region which is required to contain the indicated horizontal position with the required probability for a particular navigation mode. Similarly, the Vertical Alert Limit (VAL) is half the length of a segment on the vertical axis, with its centre being at the true position, which describes the region which is required to contain the indicated vertical position with the required probability for a particular navigation mode. As a result of our discussion, the DOP integrity flags criteria are the following:

- When the EHE exceeds the HA 95% or the VA 95% alert requirements, the CIF shall be generated.
- When the EHE exceeds the HAL or the EVE exceeds the VAL, the WIF shall be generated.

During the landing phase, a GNSS Landing System (GLS) has to be augmented by GBAS in order to achieve the RNP, as well as Lateral and Vertical Protection Levels (LPL and VPL). LPL/VPL is defined as the statistical error value that bounds the Lateral/Vertical Navigation System Error (NSE) with a specified level of confidence. In particular, for the case of Local Area Augmentation System (LAAS), which allows for multiple Differential Global Positioning System (DGPS) reference receivers (up to four) to be implemented, two different hypotheses are made regarding the presence of errors in the measurements. These hypotheses are:

H<sub>0</sub> Hypothesis – No faults are present in the range measurements (includes both the signal and the receiver measurements) used in the ground station to compute the differential corrections;

H<sub>1</sub> Hypothesis – A fault is present in one or more range measurements and is caused by one of the reference receivers used in the ground station.

Consequently, LPL and VPL are computed as follows:

$$LPL = \text{MAX} \{LPL_{H_0}, LPL_{H_1}\} \quad (2)$$

$$VPL = \text{MAX} \{VPL_{H_0}, VPL_{H_1}\} \quad (3)$$

VPL and LPL for the H<sub>0</sub> and H<sub>1</sub> hypotheses are calculated as described in [16]. The lateral and vertical accuracy (NSE 95%) and alert limits required by a GLS in the presence of LAAS, considering the continuously varying position of the aircraft with respect to the Landing Threshold Point (LTP) are given in [7]. Additionally, [7] provides the so-called Continuity of Protection Levels in terms of Predicted Lateral and Vertical Protection Levels (PLPL and PVPL). Although the definition in [7] is quite comprehensive, a generic statement is made that the PVPL and PLPL computations shall be based on the ranging sources expected to be available for the duration of the approach. In other terms, it is implied that the airborne subsystem

shall determine which ranging sources are expected to be available, including the ground subsystem's declaration of satellite differential correction availability (satellite setting information). Unfortunately, this generic definition does not address the various conditions for satellite signal losses associated to specific aircraft manoeuvres (including curved GLS precision approaches). Therefore, it is suggested that an extended definition of PLPL and PVPL is developed taking into account the continuously varying aircraft-satellite relative geometry (masking envelope). In particular, when the current aircraft manoeuvre will lead to less than 4 satellites in view or unacceptable accuracy degradations, the CIF shall be generated. Following our discussion, the additional integrity flags criteria adopted for GLS in the presence of LAAS are the following:

- When the PLPL exceeds LAL or PVPL exceeds the VAL, the CIF shall be generated.
- When the LPL exceeds the LAL or the VPL exceeds the VAL, the WIF shall be generated.

Multipath integrity flags were defined using the Early-Late Phase (ELP) observable and the range error [8]. As described in [2], the multipath integrity flags criteria are the following:

- When the ELP exceeds 0.1 radians, the caution integrity flag shall be generated.
- When the multipath range error exceeds 1 meter, the warning integrity flag shall be generated.

In order to define the integrity thresholds associated with Doppler and fading effects, a dedicated analysis of the GNSS receiver tracking performance was required. When the GNSS measurement errors exceed certain thresholds, the receiver loses lock to the satellites. Since both the code and carrier tracking loops are nonlinear, especially near the threshold regions, only Monte Carlo simulations of the GNSS receiver in different dynamics and SNR conditions can determine the receiver tracking performance [6, 9, 10]. Nevertheless, some conservative rule of thumbs that approximate the measurement errors of the GNSS tracking loops can be used. Numerous sources of measurement errors affect the Phase Lock Loop (PLL) and the Frequency Lock Loop (FLL). However, for our purposes, it is sufficient to analyze the dominant error sources in each type of tracking loop. Considering a typical GNSS receivers employing a two-quadrant arctangent discriminator, the PLL threshold is given by [6]:

$$3\sigma_{\text{PLL}} = 3\sigma_j + \theta_e \leq 45^\circ \quad (4)$$

where:

$\sigma_j$  = 1-sigma phase jitter from all sources except dynamic stress error;

$\theta_e$  = dynamic stress error in the PLL tracking loop.

Frequency jitter due to thermal noise and dynamic stress error are the main errors in a GNSS receiver FLL. The receiver tracking threshold is such that the 3-sigma jitter must not exceed one-fourth of the frequency pull-in

range of the FLL discriminator. Therefore, the FLL tracking threshold is [6]:

$$3\sigma_{FLL} = 3\sigma_{tFLL} + f_e \leq 1/4T \text{ (Hz)} \quad (5)$$

where:

$3\sigma_{FLL}$  = 3-sigma thermal noise frequency jitter;

$\sigma_{tFLL}$  = dynamic stress error in the FLL tracking loop.

Regarding the code tracking loop, a conservative rule-of-thumb for the Delay Lock Loop (DLL) tracking threshold is that the 3-sigma value of the jitter due to all sources of loop stress must not exceed the correlator spacing ( $d$ ), expressed in chips. Therefore [6]:

$$3\sigma_{DLL} = 3\sigma_{tDLL} + R_e \leq d \text{ (chips)} \quad (6)$$

where:

$\sigma_{tDLL}$  = 1-sigma thermal noise code tracking jitter;

$R_e$  = dynamic stress error in the DLL.

The Phase Lock Loop (PLL), FLL and DLL error models described in [2] allow determining the  $C/N_0$  corresponding to the receiver tracking thresholds. The integrity flag criterion applicable to the ABIA system is:

$$\left(\frac{c}{N_0}\right)_{\text{Threshold}} = \max \left[ \left(\frac{c}{N_0}\right)_{\text{PLL}}, \left(\frac{c}{N_0}\right)_{\text{FLL}}, \left(\frac{c}{N_0}\right)_{\text{DLL}} \right] \quad (7)$$

where:

$(C/N_0)_{\text{PLL}}$  = Minimum  $C/N_0$  for PLL tracking;

$(C/N_0)_{\text{FLL}}$  = Minimum  $C/N_0$  for FLL tracking;

$(C/N_0)_{\text{DLL}}$  = Minimum  $C/N_0$  for DLL tracking.

Numerical solutions of Eqs. (4), (5) and (6) show that the weak link in unaided avionics GNSS receivers is the carrier tracking loop threshold (greater sensitivity to dynamics stress). Therefore, the  $(C/N_0)_{\text{PLL}}$  threshold can be adopted in these cases. In general, when the PLL loop order is made higher, there is an improvement in dynamic stress performance. Therefore, third order PLL are widely adopted in avionics GNSS receivers. Assuming 15 to 18 Hz noise bandwidth and 5 to 20 msec predetection integration time (typical values for avionics receivers), the rule-of-thumb tracking threshold for the PLL gives 25 to 28 dB-Hz. Additionally, in aided avionics receiver applications, the PLL tracking threshold can be significantly reduced by using external velocity aiding in the carrier tracking loop. With this provision, a tracking threshold of approximately 15 to 18 dB-Hz can be achieved. Using these theoretical and experimental threshold values, we can also calculate the receiver Jamming-to-Signal (J/S) performance for the various cases of practical interest, as described in [1]. When available, flight test data collected in representative portions of the aircraft operational flight envelope (or the results of Monte Carlo simulation) shall be used. Taking an additional 5% margin on the 3-sigma tracking thresholds for the CIF, the following additional criteria are introduced for the ABIA integrity thresholds:

- When either  $42.25^\circ \leq 3\sigma_{\text{PLL}} \leq 45^\circ$  or  $0.2375T \leq 3\sigma_{\text{FLL}} \leq 0.25T$  or  $0.05d \leq 3\sigma_{\text{DLL}} \leq d$ , the CIF shall be generated.

- When either  $3\sigma_{\text{PLL}} > 45^\circ$  or  $3\sigma_{\text{FLL}} > 1/4T$  or  $3\sigma_{\text{DLL}} > d$  the WIF shall be generated.

In avionics receivers, lock detectors are used to assess if the satellite signals are being tracked or not tracked. Code lock detection is very similar to estimating the received  $C/N_0$ , inferring that the receiver is operating on or near the correlation peak. Knowledge of code lock is obviously parallel to the knowledge of received signal power. The receiver's code-correlation process has to raise the signal out of the noise. The spread spectrum processing gain ( $G_p$ ) is defined as the ratio of the spread bandwidth to the unspread (baseband) bandwidth and is expressed in dB. The post-correlation signal-to-noise ratio can be calculated by [12]:

$$(S/N)_{\text{post-corr.}} = (S/N)_{\text{pre-corr.}} + G_p \quad (8)$$

When the receiver code is aligned with the transmitted code, the signal power at the band pass output is crushed into approximately 100 Hz of bandwidth. The processing gain can be calculated from:

$$G_p = 10 \log \left( \frac{2C_R}{T_D} \right) \text{ (dB)} \quad (9)$$

where  $C_R$  is the chipping rate and  $T_D$  is the data period. For the C/A-code this works out to be about 43 dB. The TORNADO-IDS receiver has a cut off value at 10 dB, which means that if the value is less than this the satellite signal level is too low to be used in the positioning computations [11]. Therefore, an additional threshold to be accounted for is:

$$S/N_{\text{post-corr.}} = S/N_{\text{pre-corr.}} + G_p \geq 10 \text{ dB} \quad (10)$$

During experimental flight test activities performed with unaided L1 C/A code avionics receivers, it was also found that, in a variety of dynamics conditions, a  $C/N_0$  of 25 dB-Hz was sufficient to keep tracking of the satellites [12]. Consequently, taking a 2 dB margin for the CIF, the following additional criteria are adopted for the TORNADO S/N integrity flags:

- When the  $C/N_0$  is less than 27dB-Hz or the difference between the S/N and the processing gain is less than 12 dB, the CIF shall be generated.
- When the  $C/N_0$  is less than 25dB-Hz or the difference between the S/N and the processing gain is less than 10 dB, the WIF shall be generated.

## 2.2 ABIA Flight Path Optimisation Module

Optimising a trajectory for integrity based navigation is a standard optimisation problem that can be solve like all optimal control problem using a variety of direct or indirect derived methods. The optimisation problem is depicted in Fig. 4

Fig. .

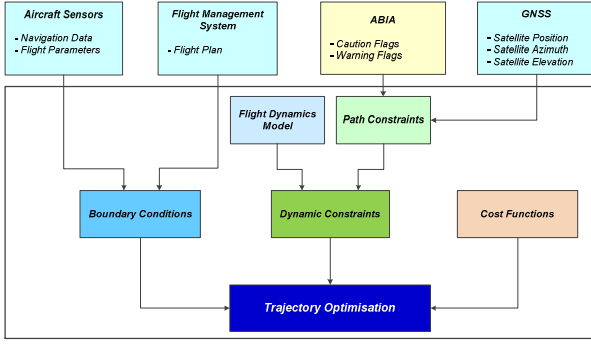


Fig. 4. Trajectory optimization problem.

All the standard components of an optimization problem are used. A flight dynamic model of the aircraft gives the dynamic constraints and allows creating a trajectory that will be flyable by the aircraft. The integrity degradations and the current GNSS parameters define a certain number of path constraints. They ensure that integrity degradations will be avoided on the whole trajectory. Then boundary conditions include minimal, maximal, initial and final values for the entire state and command variable. They are given by the aircraft sensors, which relate the current flight parameters, and by the FMS, which gives the information from the flight plan. The cost function is the performance criterion to minimize. All the necessary constraint for the integrity degradations are already included in the path constraint, therefore the time is minimized. This choice is made for simplicity and because only the integrity navigation optimization is considered in this research, but more complex criterion could be set based on aircraft performances.

### 2.2.1 Dynamics Model

The aircraft dynamics model used is a three dimensional symmetric flight, unsteady model. A 3-Degree of Freedom (3-DoF) model with variable mass is adopted. The full set of motion equations is:

$$\frac{dV}{dt} = \frac{T}{m} \cos \alpha - \frac{D}{m} - g \sin \gamma \quad (11)$$

$$\frac{d\gamma}{dt} = \left( \frac{T}{mV} \sin \alpha + \frac{L}{mV} \right) \cos \varphi - \frac{g}{V} \cos \gamma \quad (12)$$

$$\frac{d\psi}{dt} = (T \sin \alpha + L) \frac{\sin \varphi}{mV \cos \gamma} \quad (13)$$

$$\frac{dm}{dt} = -s_{sfc} T \quad (14)$$

$$\frac{d\phi}{dt} = \frac{V \cos \gamma \cos \psi}{(r_m + h)} \quad (15)$$

$$\frac{d\theta}{dt} = \frac{V \cos \gamma \sin \psi}{\cos \phi (r_t + h)} \quad (16)$$

$$\frac{dh}{dt} = V \sin \gamma \quad (17)$$

where:

- $m$  = Aircraft mass;
- $V$  = Aerodynamic speed;
- $T$  = Thrust magnitude;
- $\alpha$  = Angle of attack;

- $h$  = Altitude;
- $L$  = Lift magnitude;
- $D$  = Drag;
- $g$  = Gravity acceleration;
- $\gamma$  = Flight path angle (FPA);
- $\phi$  = Bank or roll angle;
- $\psi$  = Heading angle;
- $s_{sfc}$  = Specific fuel consumption;
- $\Phi$  = Geodetic latitude;
- $\theta$  = Geodetic longitude;
- $r_M$  = Meridional radius of curvature;
- $r_T$  = Transverse radius of curvature.

Additionally aerodynamic and propulsion parameters are calculated separately. Lift and drag are computed using standard formula.

$$L = \frac{1}{2} \rho V^2 C_L S \quad (18)$$

$$D = \frac{1}{2} \rho V^2 C_D S \quad (19)$$

where:

- $C_L$  = Lift coefficient;
- $C_D$  = Drag coefficient;
- $S$  = Reference area;
- $\rho$  = Air density.

The lift and drag coefficient are calculated from:

$$C_L = C_{L0} + C_L^\alpha \alpha \quad (20)$$

$$C_D = C_{D0} + \frac{(C_L - C_{LmD})^2 S}{\pi Ob^2} \quad (21)$$

where:

- $C_{L0}$  = Lift coefficient at zero angle-of attack;
- $C_L^\alpha$  = First order alpha derivative;
- $C_{D0}$  = Minimum drag coefficient;
- $C_{LmD}$  = Lift Coefficient at minimum drag;
- $O$  = Oswald's coefficient;
- $b$  = Wing span.

### 2.2.2 Path Constraints

The majority of the GNSS integrity degradations depend on the relative position of the GNSS receiver antenna and each satellite. The relative movement between the GNSS receiver antenna and the satellite is also crucial. Therefore degradations related to one satellite do not affect the system with the same manner or intensity as the others. A loss of integrity occurs if a combination of several degradations from different satellites takes place at the same instance. The CIF/WIF thresholds defined for the antenna obscuration, Doppler shift, multipath, carrier, interference and satellite geometry degradations are precisely capable of detecting combination of such degradations. A potential CIF or WIF is produced based on the current values of the aircraft flight parameters (position, Euler angles, and velocity), the satellite parameters (position and velocity), and the given thresholds [2]. An individual CIF or WIF is produced with respect to each satellite of the constellation. An overall CIF is triggered if there are less than 5 satellites remaining without an individual

CIF and an overall WIF is triggered if less than 4 satellites are remaining without an individual WIF. In order to constrain the trajectory optimization process, dynamic constraint criteria are adopted. An analysis of the different type of degradations results in inferring that a common criterion based on satellite elevation variation in the body frame can be adopted.

### 2.2.3 Boundary Conditions

The minimum and maximum values for each state and control variable define the interval allowed during the optimization process. The range has a direct impact on the duration and the result of the simulation. The boundary values are determined based on four main sources including:

- Current Flight Parameters (CFP) that define the initial conditions when the optimization process is started at the WIF generation time step.
- Flight Plan (FP), which defines the final conditions of the optimization problem, which are essential to determine the Trajectory Change Point (TCP) where the UAV can re-join with the initially planned trajectory.
- Aircraft performance, which dictate the minimum and maximum values for the state and control variables.
- Current satellite data that provide the boundary for the path constraint.

### 2.2.3 Mathematical Criterion

The elevation and azimuth angles in body frame (blue) are depicted in Fig. 5. **Error! Reference source not found.**

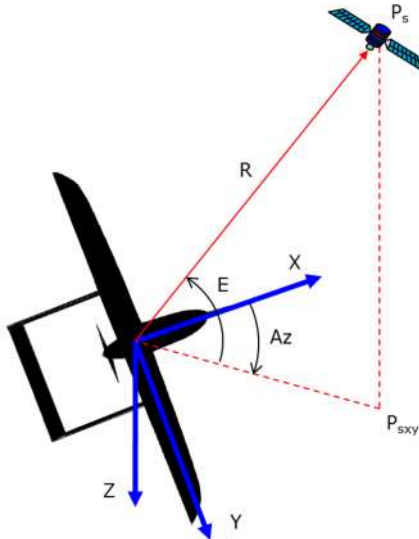


Fig. 5. Elevation and azimuth in body frame.

where:

$P_S$  = Satellite position;

$P_{SXY}$  = Satellite position in XY frame;  
 $R$  = Line of sight vector;  
 $E$  = Elevation angle;  
 $Az$  = Azimuth angle.

The direction of rotation of the elevation and azimuth angle are given by the right-hand rule. Considering top view of the UAV, when the elevation angle increases in the positive direction (going up), the azimuth is rotating in a clockwise direction. The elevation angle in the body frame is computed using the simple trigonometry relation given by:

$$E = \sin^{-1} \left( \frac{R_z}{\|R\|} \right) \quad (22)$$

where  $R_z$  is the Z-axis component of the line of sight vector. In order to use as a dynamic constraint for trajectory optimisation, the elevation angles are associated with Euler angles by converting the Line-of-Sight (LOS) vector from the East-North-Up (ENU) reference frame to the body frame. The position of the UAV and satellite is given in the ENU frame, so the LOS vector is computed using:

$$R = P_S - P_R \quad (23)$$

where  $P_R$  is the receiver position.

The flight path optimisation algorithm is initiated when degradation in integrity is predicted or detected by the IFG. The elevation and azimuth are always considered in the body frame and  $Az \in [-180^\circ; 180^\circ]$ . The successive steps involved are:

- Step 1: The satellites in view that remain without an individual integrity flag are selected and their data are extracted (position, elevation, azimuth and other information).
- Step 2: For each selected satellite, the type of flag is analysed:
  - If the flag is not due to Doppler shift, the minimum elevation limit is set with the current selected satellite's elevation angle.
  - If the flag is due to Doppler shift, the sign of the azimuth angle is compared to the sign of the bank angle. This means that if the satellite is located in the same direction of the track, the minimum elevation limit is set with the current satellite's elevation value. But if the satellite is located in the opposite direction of the track, the maximum elevation limit is set with the current satellite's elevation value.
- Step 3: After the satellite elevation limits are set, the parameters are used in the trajectory optimization suite.

## 3. SENSE-AND-AVOID SYSTEM

Both cooperative and non-cooperative SAA systems are being developed to address UAS safe integration into the non-segregated airspace [13]. The SAA capability can be defined as the automatic detection of possible

conflicts (i.e., collision threats) by the UAV platform and the implementation of avoidance manoeuvres to prevent the identified collision threats. An analysis of the available SAA candidate technologies and the associated sensors was presented in [14, 15]. An approach to the definition of encounter models and their applications on the SAA strategies is presented in [16, 17] considering both cooperative and non-cooperative scenarios. As part of our research, the possible synergies attainable with the adoption of different detection, tracking and trajectory generation algorithms were studied. Additionally, the error propagation from different sources and the impacts of host and intruders dynamics on the ultimate SAA solution were investigated [15]. The requirements for developing an effective SAA system can be derived from the current regulations applicable for the human pilot see-and-avoid capability. Table 1 summarises the SAA range and Field-of-Regard (FOR) requirements [13, 16, 18, 19].

Table 1. SAA range and FOR requirements.

Detection range requirements (NM)				
Altitude	Manned	UAS		
	Nominal pilot	Autonomous	Line-of-sight	Beyond line-of-sight
Low	2.6	1.1	1.8	1.9
Medium	4.2	1.8	2.9	3.1
High	5.7	2.8	4.1	4.3
FOR requirements (°)				
Azimuth	$\pm 110$			
Elevation	$\pm 15$			

The system detection range and FOR have to be adequate to ensure separation from the intruder to prevent a probable near mid-air collision. This criterion is also naturally applicable in the case of small UA since the vast majority of mid-air collision events occur below 3000 ft [16]. The key criteria for designing an effective SAA system are:

- The Field of View (FOV) has to be equivalent or superior to that of a pilot in the cockpit and it corresponds to primary FOV - 60° in vertical and 70° in horizontal and secondary FOV - 100° in vertical and 120° in horizontal [20].
- Common FOV/FOR for visual and thermal cameras.
- Accurate and precise intruder detection, recognition and trajectory prediction.
- Prior obstacle detection for allowing time for executing the trajectory avoidance manoeuvres.
- Effective fusion schemes for multi-sensor data augmentation, especially by tight coupling [21].
- Identification of the primary means of cooperative and non-cooperative SAA system for integrity requirements.

A number of cooperative and non-cooperative sensors/systems have been studied recently. Cooperative systems typically include TCAS (Traffic Collision Avoidance System) / ACAS (Airborne Collision Avoidance System) and Automatic Dependent Surveillance Broadcast (ADS-B). The inclusion of ADS-B in association with GNSS-based navigation systems redefines the paradigm of C-SAA in the Communication, Navigation and Surveillance (CNS) Air Traffic Management (ATM) context by allowing the share of accurate GNSS trajectory information. The non-cooperative SAA sensors are employed to detect intruders or other obstacles in the UA FOR when cooperative systems are unavailable in the intruders [22]. Optical, thermal, LIDAR, MMW Radar and acoustic sensors can be used as part of non-cooperative SAA architecture. As an example, the combined SAA architecture proposed in [15] is depicted in Fig. 6 with an identification of primary (solid line) and auxiliary sensors (dashed line) for cooperative and non-cooperative SAA tasks.

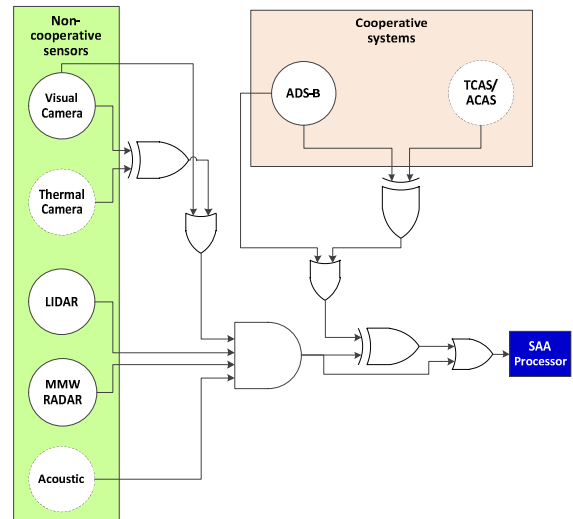


Fig. 6. SAA system architecture. Adapted from [15].

The sequential steps involved in the SAA process for executing an efficient Tracking, Deciding and Avoiding (TDA) loop are illustrated in Fig. 7.

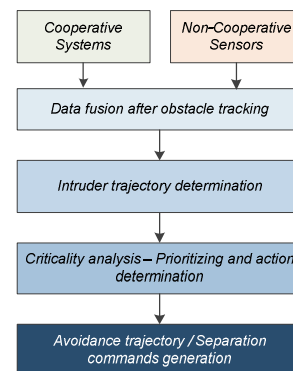


Fig. 7. SAA system process.

Criticality analysis is carried out to prioritize (i.e. to determine if a collision risk threshold is exceeded for all the tracked intruders) and to determine the action commands. If an avoidance action is required, the SAA system generates and optimises an avoidance trajectory according to a cost function defined by {minimum distance, fuel, time and closure rate} with the aid of differential geometry algorithms [16] to generate a smooth trajectory.

### 3.1 Non-Cooperative sensors

Gimballed visual and thermal cameras are used for determining position and velocity estimates of the intruders. To obtain all-weather operation, thermal imaging can be used in conjunction with the visual sensor. The proposed hardware for the camera provides an approximate FOV of 70° with a resolution of 2.0 MP. The fusion of optical sensors with other non-cooperatives sensors increases the angular accuracy. LIDAR sensor, scaled from [23], is proposed for extracting range measurements and provides a FOV of 40° in azimuth and 15° in elevation. It allows the operator to select the azimuth orientation of the FOV among three possible directions: aligned with the platform heading (normal flight envelope) or 20° left/right with respect the platform heading. This option provides an optimized coverage for turning manoeuvres at high angular speed. For stabilised obstacle detection, after image acquisition, the noise caused by the platform motion is removed. Bottom-hat morphology is performed to detect negative contrast features that correspond to the threats. Low-level tracking is achieved by utilising Ad-hoc Viterbi filtering method by employing a bank of filters. Let  $\alpha_n^b(i, j)$  be the filter output at time step,  $n$  of pixel  $(i, j)$  for the filter bank branch  $b$ , and  $I_n(i, j)$  be the greyscale level of pixel  $(i, j)$ , the Ad-hoc Viterbi filter steps, for  $1 \leq i \leq H, 1 \leq j \leq W$  and all  $n$ , are carried out. The statistical test criterion for evaluation to determine the actual presence of a collision threat is given by:

$$\gamma_n = \max_{1 \leq i \leq H, 1 \leq j \leq W} [\alpha_n(i, j)] \quad (24)$$

where  $\gamma_n$  is the comparison parameter and is equivalent to 0.75 [14]. A multi-sensor navigation and guidance system is adopted for position estimates, which includes Global Navigation Satellite System (GNSS), Micro-Electromechanical System (MEMS) Inertial Measurement Unit (IMU) and Vision Based Navigation (VBN) sensors [24, 25]. When the set threshold is exceeded and the detection is continuous, high level tracking detection is performed by using a Kalman filter. The predicted state,  $\hat{x}(t)$  at time  $t$  is given by:

$$\hat{x}(t) = \begin{bmatrix} P_x(t) \\ P_y(t) \\ V_x(t) \\ V_y(t) \end{bmatrix} = \begin{bmatrix} 1 & 0 & 1 & 0 \\ 0 & 1 & 0 & 1 \\ 0 & 0 & 1 & 0 \\ 0 & 0 & 0 & 1 \end{bmatrix} \begin{bmatrix} P_x(t-1) \\ P_y(t-1) \\ V_x(t-1) \\ V_y(t-1) \end{bmatrix} + \begin{bmatrix} \frac{t^2}{2} & 0 \\ 0 & \frac{t^2}{2} \\ t & 0 \\ 0 & t \end{bmatrix} \begin{bmatrix} a_x \\ a_y \end{bmatrix} + \varepsilon(t) \quad (25)$$

where  $P_{x,y}(t)$  is the position in the  $x$  and  $y$  directions respectively as a function of time,  $t$ .  $V_{x,y}(t)$  is the velocity in the  $x$  and  $y$  direction respectively,  $a_{x,y}(t)$  is the acceleration and  $\varepsilon(t)$  is the prediction Gaussian noise. The Kalman filter equations adopted are:

$$\hat{x}_i(k|k) = \hat{x}_i(k|k-1) + W_i(k)[z_i(k) - H_i(k)x_i(k|k-1)] \quad (26)$$

$$P_i(k|k) = P_i(k|k-1) - W_i(k)S_i(k)W_i^T(k) \quad (27)$$

where:

$$W_i(k) = P_i(k|k-1)H_i^T(k)S_i^{-1}(k) \quad (28)$$

$$S_i(k) = [H_i(k)P_i(k|k-1)H_i^T(k) + R_i(k)] \quad (29)$$

where  $H_i(k)$  represents the design matrix and  $R_i(k)$  is the measurement noise covariance matrix and  $k$  is the sample time. The Track-To-Track ( $T^3$ ) algorithm is employed for sensor fusion. The primary advantage of adopting this method is to combine the estimates instead of combining the observations from different sensors. The track fusion algorithm is defined as the weighted average variance of all the tracks and is given by:

$$\hat{x}_F(k|k) = P_F(k|k) \times \sum_{i=1}^n P_i^{-1}(k|k) \hat{x}_i(k|k) \quad (30)$$

$$P_F(k|k) = [\sum_{i=1}^n P_i^{-1}(k|k)]^{-1} \quad (31)$$

Once the tracks are fused and the states are estimated, the imminent trajectory is predicted. The errors in predicted trajectory can be derived from the quality of the measurements, reflected in the prediction error, which are expressed as:

$$\sigma^2(k + \tau|k) = \text{var}[n(k + \tau) - \hat{n}^1(k + \tau|k)] \quad (32)$$

where  $n(k + \tau)$  is the exhibited (modelled) trajectory and  $\hat{n}^1(k + \tau|k)$  is the predicted optimal trajectory at sample time  $k + \tau$ . For trajectory prediction, the obstacle centre of mass, the target orientation and the geometric shape of the uncertainty volume are determined. Once the trajectory is predicted, the Risk of Collision (ROC) is determined by calculating the probability of a near mid-air event for the predicted trajectory over the time horizon by employing Monte Carlo approximations.

### 3.2 Cooperative systems

Using ADS-B, the future position of the intruder is projected based on the current state vector. The ADS-B measurement model adopted for position and velocity estimates in x and y cardinal directions is given as:

$$Z(k) = \begin{bmatrix} 1 & 0 & 0 & 0 & 0 & 0 \\ 0 & 1 & 0 & 0 & 0 & 0 \\ 0 & 0 & 0 & 1 & 0 & 0 \\ 0 & 0 & 0 & 0 & 1 & 0 \end{bmatrix} \begin{bmatrix} \dot{x} \\ \ddot{x} \\ y \\ \dot{y} \end{bmatrix} + \begin{bmatrix} V_x(k) \\ V_x(k) \\ V_y(k) \\ V_y(k) \end{bmatrix} \quad (33)$$

Assuming the velocity components,  $V_x(k)$ ,  $V_x(k)$ ,  $V_y(k)$  and  $V_y(k)$  as being affected only by Gaussian noise with zero mean, the standard deviation is defined by the covariance matrix given by:

$$R = \begin{bmatrix} E[V_x^2] & 0 & 0 & 0 \\ 0 & E[V_x^2] & 0 & 0 \\ 0 & 0 & E[V_y^2] & 0 \\ 0 & 0 & 0 & E[V_y^2] \end{bmatrix} \quad (34)$$

where  $E[\ ]$  represents the mean. An Interacting Multiple Model (IMM) algorithm is adopted for data fusion. The IMM model is a state-of-the-art tracking algorithm when multiple kinematics behaviour is to be considered. Using this model, the state vector of the intruders is determined and this is propagated to predict the future trajectories using a probabilistic model. After computing the mixing probability, the combination of the state estimate is given by:

$$\hat{x}_F(k|k) = \sum_{i=j}^r \hat{x}^j(k|k) \mu_j(k) \quad (35)$$

where  $\mu_j(k)$  is the mode probability update. For conflict detection, the resultant covariance matrix,  $Q$  after transformation is defined as:

$$Q = R * S * R^T \quad (36)$$

where  $S$  is the diagonal covariance matrix and  $R$  represents the transformation matrix between the heading aligned frame to that of the UA host platform frame. The probability of conflict is defined as the volume below the surface of the probability density function,  $p(x,y)$  representing the conflict zone. The conflict probability,  $P_c$  is expressed as:

$$P_c = \int_{-\Delta y - \Delta y_c}^{-\Delta y + \Delta y_c} \int_{-\infty}^{+\infty} p(x,y) dx dy \quad (37)$$

where  $\Delta y + \Delta y_c$  represents the conflict separation distance and  $\Delta x_c, \Delta y_c$  correspond to the rows of the conflict boundary matrix. The conflict probability is simplified as:

$$P_c = P(-\Delta y + \Delta y_c) - P(-\Delta y - \Delta y_c) \quad (38)$$

### 3.3 Uncertainty Volume

Error analysis is performed to determine the overall uncertainty volume in the airspace surrounding the intruder tracks. This is accomplished by considering both the navigation and the tracking errors affecting the

measurements and translating them to unified range and bearing uncertainty descriptors. In order to quantify the errors, let  $\sigma_{Ex}$ ,  $\sigma_{Ey}$  and  $\sigma_{Ez}$  represent the standard deviation of the navigation error ( $\sigma_{nx}$ ,  $\sigma_{ny}$ ,  $\sigma_{nz}$ ) or the tracking error ( $\sigma_{tx}$ ,  $\sigma_{ty}$ ,  $\sigma_{tz}$ ) in the x, y and z cardinal directions respectively. Using a spherical coordinates frame with origin at the host UA centre of mass, the range and bearing errors associated with the intruder tracking process is transformed into a local Cartesian coordinate frame (either host or intruder body frame). The error ellipsoid is defined as [15]:

$$\frac{x^2}{\sigma_{Ex}^2} + \frac{y^2}{\sigma_{Ey}^2} + \frac{z^2}{\sigma_{Ez}^2} = 1 \quad (39)$$

With respect to the obtained navigation and tracking error ellipsoids, spherical harmonics coefficients are determined. Let  $r(\theta, \psi)$  represent the smooth function defined on the ellipsoid and the parameterisation is given by:

$$r(\theta, \psi) = \sum_{l=0}^{\infty} \sum_{m=-l}^l X_{lm} Y_{lm}(\theta, \psi) \quad (40)$$

The function  $r(\theta, \psi)$  is limited to a number of  $N$  finite coefficients.  $X_{lm}$  is a factor and the function  $Y_{lm}(\theta, \psi)$  is the spherical harmonic function and is given by:

$$Y_{lm}(\theta, \psi) = \sqrt{\frac{(2l+1)(l-m)!}{4\pi(l+m)!}} P_{lm} \cos(\theta) e^{im\psi} \quad (41)$$

where  $P_{lm}$  represents the Legendre functions. Expanding  $e^{im\psi}$  as  $C_{lm} \cos(m\psi) + i S_{lm} \sin(m\psi)$ , we have  $C_{lm}$  and  $S_{lm}$  defined as the spherical harmonic coefficients. The spherical harmonic coefficients are obtained as [26]:

$$S_{lm} = 0; \quad l, m \in N \quad (42)$$

$$C_{lm} = 0; \quad l, m \in 2N + 1 \quad (43)$$

and for all other  $l, m$ :

$$C_{lm} = \frac{3}{a^l} \frac{(\frac{1}{2})^l (\frac{l}{m})^{l(2-\delta_{0m})}}{2^m (l+3)(l+1)!} \times \quad (44)$$

$$\sum_{i=0}^{(l-m)/4} \frac{(a^2 - b^2)^{(m+4i)/2} [c^2 - (\frac{1}{2})(a^2 - b^2)]^{(l-m-4i)/2}}{16^i (\frac{l-m-4i}{2})! (m + \frac{2i}{2})! i!}$$

where  $\delta_{0m}$  is the Kronecker symbol and  $(a, b, c)$  represents the semi-major radius of the navigation or tracking error ellipsoid. Both navigation and tracking error ellipsoids are generated and the overall uncertainty volume is obtained by combining the two error ellipsoids. A notional example of the resulting uncertainty volume for uncorrelated measurements (obtained by inflating the navigation ellipsoid with the tracking error components) is illustrated in Fig. 8.



made objects (e.g., buildings). The Doppler Simulator Module (DSM) was used to calculate the Doppler shift by processing ADS and GCS inputs. The Multipath Analysis Module (MAM) processed the 3DM, TEM, GCS and ADS inputs to determine multipath contributions from the aircraft (wings/fuselage) and from the terrain/objects close to the aircraft. The Obscuration Analysis Module (OAM), and was used to compute the GNSS antenna(e) masking matrixes for all aircraft manoeuvres with inputs from the 3DM, GCS and ADS. The nominal link budget of the direct GNSS signals received by the aircraft in the presence of ionospheric and tropospheric propagation disturbances was evaluated using SAM. The Integrity Flags Simulator (IFS) used a set of predefined threshold parameters to trigger the generation of both caution and warning flags associated with antenna obscuration, Doppler shift, multipath, SNR and satellite geometry degradations.

### 6.1 GNSS Constellation Simulator

The GNSS constellation simulator (GCS) was developed to calculate GNSS satellite position and velocity in the Earth-Centred Earth-Fixed (ECEF) reference frame and to obtain satellite visibility data from any point along the aircraft flight trajectory. The initial version of the GCS was implemented in MATLAB<sup>®</sup> to simulate GPS and GALILEO constellations. However, the GCS was developed as a flexible tool capable to incorporate other current and likely future GNSS constellations (GLONASS, COMPASS, IRNSS, QZSS, etc.), including space-based regional and global augmentation systems. The satellite position and velocity are calculated from the Kepler's laws of orbital motion using either the YUMA or SEM almanac data [30, 31].

### 6.2 Aircraft 3-D Model

Various geometric parameters were extracted from the literature to draw a detailed CATIA model of the AEROSONDE UAV [32, 33, 34]. The AEROSONDE 3-D CATIA model obtained is illustrated in Fig. 10.

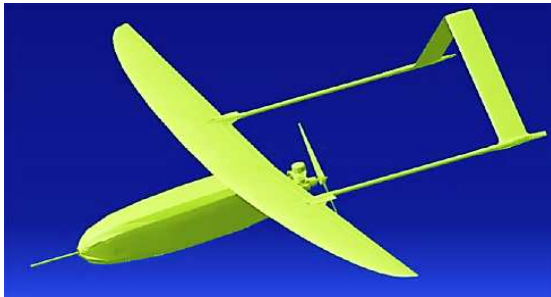


Fig. 10. AEROSONDE 3-D CATIA model.

To calculate the antenna masking matrix and the corresponding satellite visibility conditions, the antenna location were included in the model. The location of

the AEROSONDE GPS antenna extracted from the literature is shown in Fig. 11.

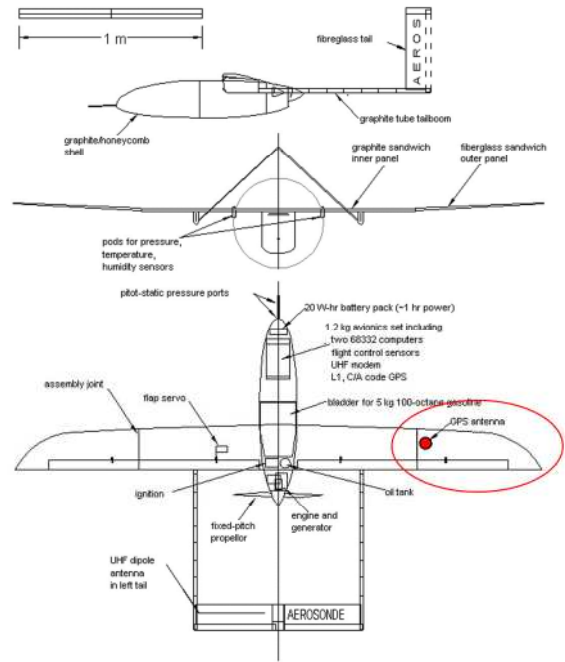


Fig. 11. AEROSONDE antennae locations. Adapted from [35, 36].

The antenna-satellite LOS is measured in the antenna frame (i.e., origin at the antenna focal point) and the transformation from body-frame to antenna frame is obtained from:

$$F_{\text{antenna}} = F_{\text{body}} + T_{\text{body}}^{\text{antenna}} \quad (\text{m}) \quad (46)$$

For the AEROSONDE UAV, the single antenna transformation matrix is:

$$T_{\text{body}}^{\text{antenna}} = \begin{bmatrix} 0.34 \\ 1.69 \\ 0.43 \end{bmatrix} \quad (\text{m}) \quad (47)$$

### 6.3 Satellite Masking Analysis

Due to the manoeuvres of the UAV, the wings, tail and fuselage will obscure some satellites during the flight. Fig. 12 shows the structure of the Satellite Masking Analysis (SMA) module.

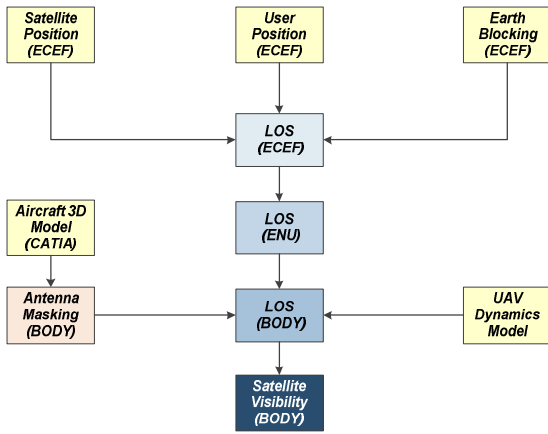


Fig. 12. GNSS satellite obscuration simulator.

Taking into account the aircraft shape (CATIA 3-D model), the aircraft flight dynamics and the information provided by the GCS, an Antenna Masking Matrix (AMM) is generated for the different flight phases. To automate the process of AMM generation, Automatic Masking Profile Computation (AMPC) software was developed. The AMPC software populates a database (look up tables) containing the obscuration information of GNSS satellite signals for different aircraft roll and pitch angles. This is accomplished by implementing two different modules in the AMPC: the first is used to transform the aircrafts CAD model in a mesh of small triangular surfaces that allows straightforward computations of line/surface intersections in a MATLAB® environment; the second is used to rotate the aircraft in pitch and roll (bank), and to calculate the intersections between the aircraft structure (i.e., fuselage, wings and tail) and the line-of-sight (LOS) to all satellites in view as illustrated in Fig. 13.

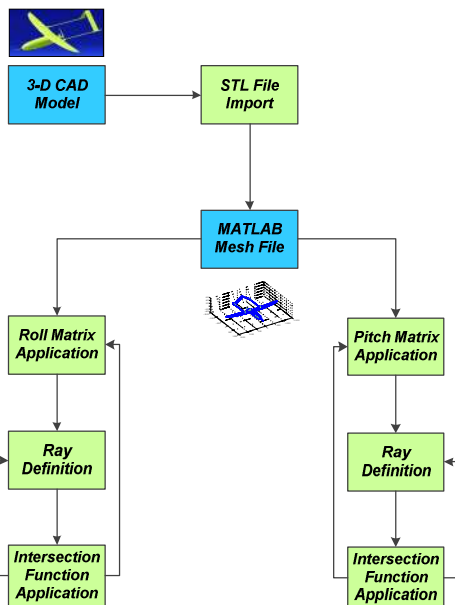


Fig. 13. AMPC logic diagram.

After creating the 3-D aircraft surface model, the corresponding CAD file was transformed in a Stereolithography (STL) file format. An STL file is a convenient representation of a complex 3D surface geometry, made by a number of oriented triangles (mesh). Each of these triangles is described by two elements: the first is a unit normal vector to the facet; the second element is a set of three points listed in counter clockwise order representing the vertices of the triangle. This representation is ideally suited for the ABIA simulation environment. As an example, the AEROSONDE mesh imported and plotted in MATLAB® is illustrated in Fig. 14.

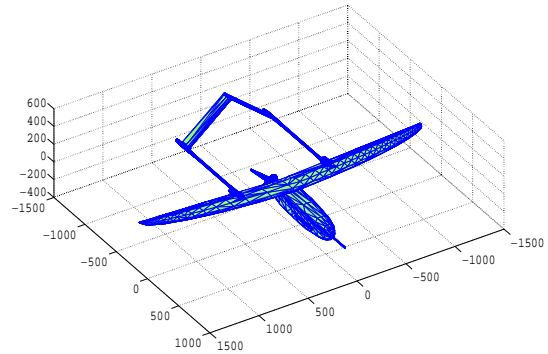


Fig. 14. AEROSONDE mesh in MATLAB®.

Using this representation, the AMMs in pitch and roll are generated calculating all possible intersections of the aircraft body (all triangular surfaces) with the LOS antenna-satellites (Fig. 15).

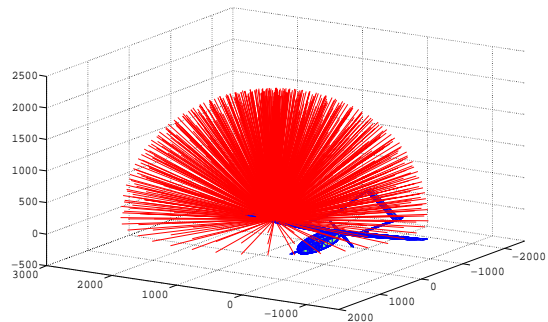


Fig. 15. AEROSONDE masking profile simulation.

In order to generate CIF/WIF associated to critical UAV antenna masking conditions, a dedicated analysis is required taking into account the simultaneous variation of pitch and bank. An example of the resulting Global Masking Envelope (GME) taking into account both bank (B) and pitch (P) angle variations is shown in Fig. 16.

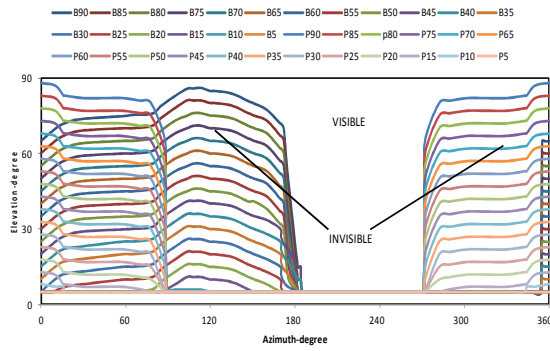


Fig. 16. Global masking envelope.

Besides the GME, other factors influence the satellite visibility. In general, a satellite is geometrically visible to the GNSS receiver only if its elevation in the antenna frame is above the Earth horizon and the antenna elevation mask. It should be noted that even high performance avionics GNSS antennas have a gain patterns that is typically below -3dB at about 5 degrees elevation [37] and, as a consequence, their performance become marginal below this limit. In order to determine if a satellite is obscured, the LOS of the satellite with respect to the antenna phase centre has to be determined. To calculate the satellite azimuth and elevation with respect to the antenna the transformation matrix between ECEF (Earth Centred Earth Fixed) and the antenna frame must be applied. This transformation is obtained as follows:

$$T_E^A = T_b^a * T_N^b * T_E^N \quad (48)$$

where  $T_b^a$  is the transformation matrix between the aircraft body frame and the antenna frame,  $T_N^b$  is the transformation matrix from ENU (East-North-Up) to body frame, and  $T_E^N$  is the ECEF to ENU transformation matrix.

#### 6.4 IFG Simulation

In order to validate the design of the ABIA IFG module, a MATLAB<sup>®</sup> simulation activity was performed employing the algorithms developed during this research. The simulated AEROSONDE UAV trajectory included the following flight phases:

- Climb phase (0-300s);
- Turning climb phase (300-600s);
- Straight and level (cruise) phase (600-900s);
- Level turn phase (900-1200s)
- Turn and descend phase (1200-1500s);
- Descend (straight approach) phase (1500-1800s);

The combined GPS/GALILEO constellation was simulated and the GNSS receiver tracking loops were modelled with a flat random vibration power curve from 20Hz to 2000Hz with amplitude of  $0.005g^2/Hz$  and the oscillator vibration sensitivity  $S_v(f_m) = 1 \times 10^{-9}$  parts/g. All CIFs and WIFs relative to antenna masking, geometric accuracy degradations, SNR, multipath and Doppler shift were generated. The main results

obtained with the simulated GPS constellation are shown in Table 2. In some cases, the CIF was generated but it was not followed by the WIF (this was due to a temporary adverse relative geometry not leading to GNSS signal losses). During the level turn and turning descent phases, the CIF was followed by the WIF. It was also observed that the CIF was always triggered at least 2 seconds before the successive WIF onset (up to 13 seconds in one case during the turning descent phase).

These results are consistent with previous ABIA research on manned aircraft applications [1, 2, 3] and corroborate the validity of the models developed for the CIF/WIF thresholds. It is evident that the availability of a usable CIF represents a significant progress in this research with the potential for both manned aircraft and UAVs to recover from mission- and safety-critical flight conditions potentially leading to GNSS data losses. Therefore, it is envisaged that a properly designed ABIA FPM could take full advantage of this predictive behaviour, allowing the UAV to correct its flight trajectory/attitude in order to avoid the occurrence of the critical GNSS data losses. Additionally, it is possible that this predictive behaviour be exploited in the pursuit of a GNSS based auto-landing capability.

Table 2. GPS constellation simulation results.

	CIF	WIF
Climb	---	---
Turning Climb	334-374s, 426-446s 517-558s	---
Cruise	874-900s	---
Level Turn	901-1200s	903-906s, 913s, 920-924s, 930-931s, 938-942s, 948-949s, 956-959s, 966-967s, 974-977s, 984-985s, 992-995s, 1002-1003s, 1110-1113s, 1020-1021s, 1028-1031s, 1128-1129s, 1136-1139s, 1146-1147s, 1154-1157s, 1164-1165s, 1172-1175s, 1182-1183s, 1190-1192s, 1200s
Turning Descent	1201-1441s, 1448-1464s, 1471-1487s 1494-1500s	1204s, 1223-1224s, 1247-1249s, 1272-1273s, 1296-1297s, 1320-1321s, 1344-1367s, 1368s, 1391-1392s, 1414-1415s, 1438-1439s, 1461-1462s, 1484-1485s
Descent	1503-1800s	---

These results contribute to corroborate the validity of the models developed for the CIF/WIF thresholds. It was also observed that the CIF was always triggered at least 2 seconds before the successive WIF onset. This evidence is particularly important for the ABIA system

design. In fact, it is evident that the availability of a usable CIF represents a significant progress in this research with the potential for both manned aircraft and UAVs to recover from mission- and safety-critical flight conditions potentially leading to GNSS data losses. Therefore, it is envisaged that a properly designed ABIA FPM could take full advantage of this predictive behaviour, allowing the UAV to correct its flight trajectory/attitude in order to avoid the occurrence of the critical GNSS data losses. Additionally, it is possible that this predictive behaviour be exploited in the pursuit of a GNSS based auto-landing capability.

### 6.5 IFG/FPM Simulation

Simulation activities were also carried out to validate the IFG/FPM integration. An initial trajectory was used as a reference and was obtained by using the AEROSONDE 3-DOF dynamics model. The resultant scenario is depicted in Fig. 17 Fig.

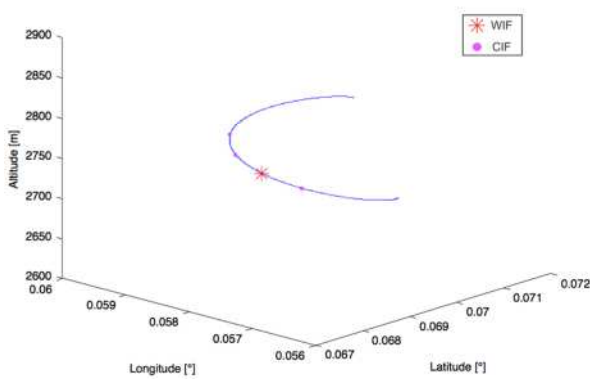


Fig. 17. Simulation scenario.

The trajectory is a turning descent path with a constant pitch angle of  $-5^\circ$  of pitch, a constant bank angle of  $-40^\circ$ , and a constant throttle of 2000 RPM. All the state and command variables for the entire path are plotted in Appendix A. A first predictive caution is generated, then at the next time step of the degradation analysis another predictive caution signal is generated, because the thresholds for integrity degradations are still not exceeded. Finally at the second analysis point after the first caution signal the integrity degradation happens and is detected. A new trajectory that avoids GNSS degradation can be optimized starting when the first predictive caution is generated. Pseudospectral optimization was used to solve the optimization problem. The resulting trajectory, also tested with the same integrity degradation detection model, is shown in Fig. 18

Fig.

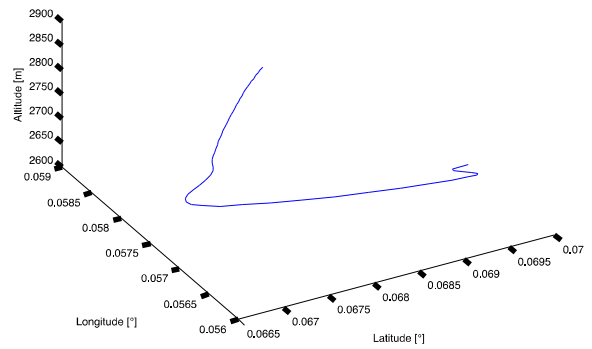


Fig. 18. Optimised trajectory without any integrity degradations.

To avoid degradations and at the same time to satisfy the path constraints with the conditions set on satellite elevation angle, the optimised trajectory was obtained by decoupling the pitch and the bank angles. It was observed that pitch down and turn left commands were performed. The effect on the satellite elevation angle in the body frame is illustrated in Fig. 19 and 20. It was observed that before optimisation, the elevation drops significantly after the first integrity degradation prediction (represented as dots in Fig. 19), which leads to an integrity loss. After optimisation, it was observed that the elevation angle is high enough to prevent the occurrence of the loss of integrity.

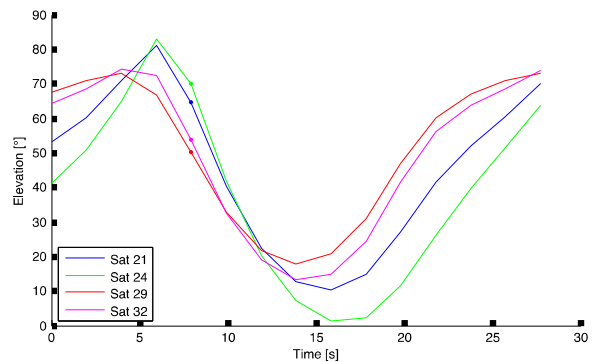


Fig. 19. Elevation of the satellites before optimisation.

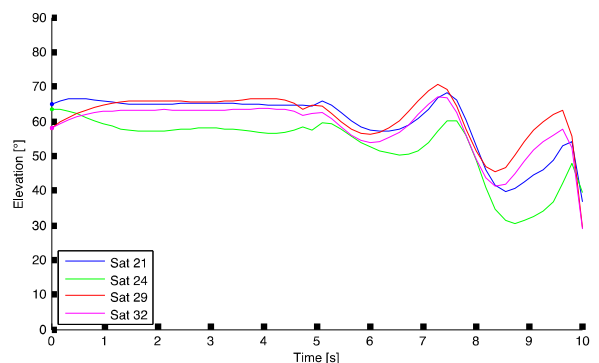


Fig. 20. Elevation of the satellites after optimisation.

### 6.6 ABIA/SAA Simulation

The ABIA integration into an existing UAV SAA architecture was studied in cooperative and non-

cooperative SAA scenarios. The test platforms used were 3DoF aircraft dynamics models:

- AEROSONDE UAV (ABIA host platform) ans
- AIRBUS 320 (A320) and AEROSONDE UAV intruders.

In all the scenarios, an avoidance volume (sum of navigation and tracking errors) was generated by the SAA system [15]. Pseudospectral (PSO) or constrained differential geometric optimization (DGO) techniques were used to generate the new trajectory based on the available time to conflict (host entering the avoidance volume). The avoidance trajectory was initiated by the SAA system when the probability of collision exceeded the required threshold value. Time and fuel were used in the cost functional, the dynamic model as dynamic constraint, and the elevation criteria as path constraints for both PSO and DGO techniques. Boundary conditions were set from the value of the flight parameters at CIF time step. A collision avoidance trajectory free of GNSS integrity degradation was generated. Fig. 21 illustrates the cooperative SAA test scenario wherein two AEROSONDE (1 ABIA host platform and 1 intruder) UAV are 90° off track at the same Flight Level (FL). The collision is detected and resolved and as a result the host and intruder UAVs avoid colliding in mid-air. The host UAV platform equipped with ABIA/SAA is able to generate an avoidance trajectory without any CIF/WIF occurrences. As can be seen from Fig. 21, the host UAV SAA only avoidance trajectory and ABIA/SAA avoidance trajectory have a different re-join point on the original track.

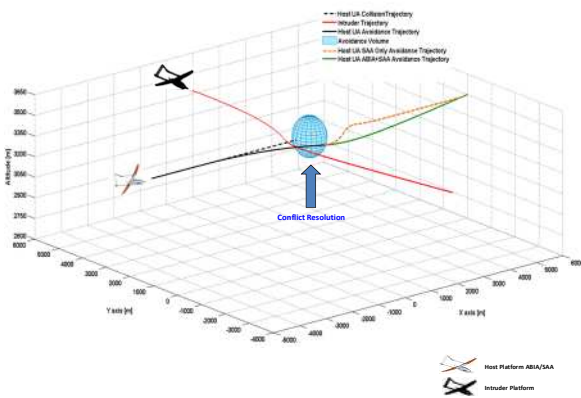


Fig. 21. 2 UAV 90° collision cooperative SAA scenario.

Three different points are shown on the ABIA/SAA host platform trajectory in Fig. 22:

- SAA Break-off Point: Corresponding to the point where the host UA initiates the avoidance trajectory (commanded by the SAA system). The cost function criteria adopted in this case is minimum time.
- SAA Safe Manoeuvring Point: Corresponding to the point where the host UAV can manoeuvre safely (any manoeuvre within its operational flight

envelope) has 0 ROC. From this point onwards the SAA cost function criteria switches to minimum time and minimum fuel to get back on the original (desired) track.

- ABIA Re-join Point: Corresponding to the point where the host UAV re-joins the original (desired) track without GNSS data degradations.

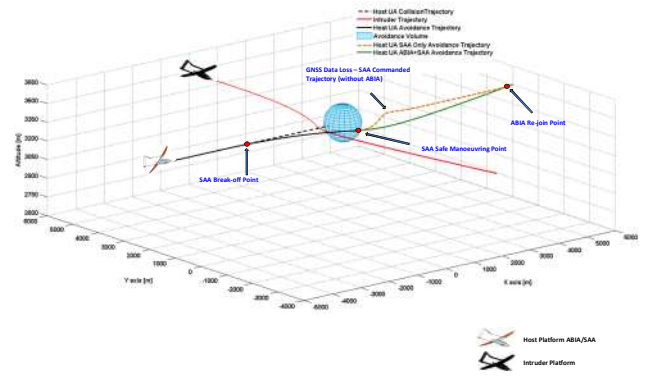


Fig. 22. Illustration of reference points.

The horizontal separation and predicted conflict probability in this case is shown in Fig. 23 and 24 respectively.

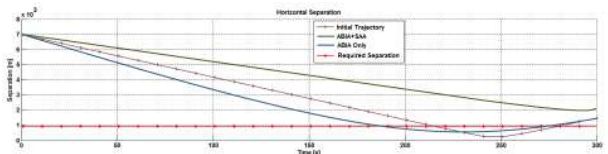


Fig. 23. Obtained horizontal separation.



Fig. 24. Predicted conflict probability.

Fig. 25 illustrates the non-cooperative SAA test scenario wherein AEROSONDE (ABIA host platform) UAV and an A320 are on the same FL but are 90° off track to each other.

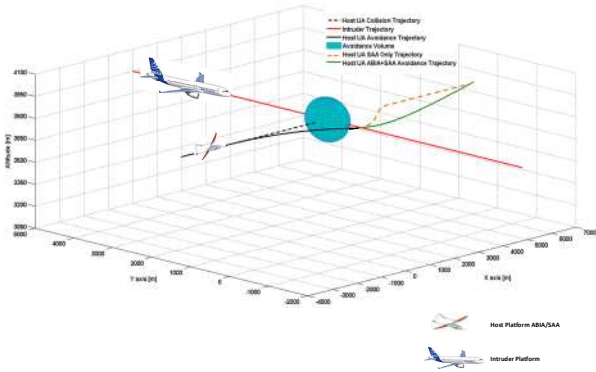


Fig. 25. UAV 90° collision non-cooperative SAA scenario.

The horizontal and vertical separation obtained is illustrated in Fig. 26.

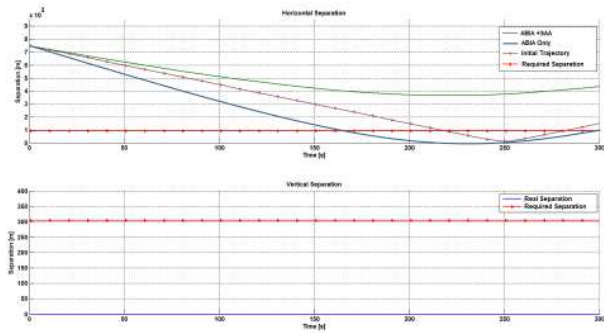


Fig. 26. Obtained horizontal and vertical separation.

Fig. 27 illustrates the cooperative SAA test scenario wherein AEROSONDE (ABIA host platform) UAV and two intruders (AEROSONDE UAVs) are on the same FL. One intruder UAV is 90° off track and the other is on a head-on collision with the host UAV. The horizontal and vertical separation obtained with respect to intruder 1 and 2 are illustrated in Fig. 28 and 29 respectively.

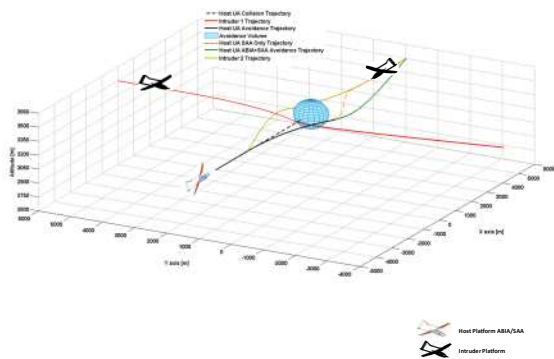


Fig. 27. 3 UAV collision cooperative SAA scenario.

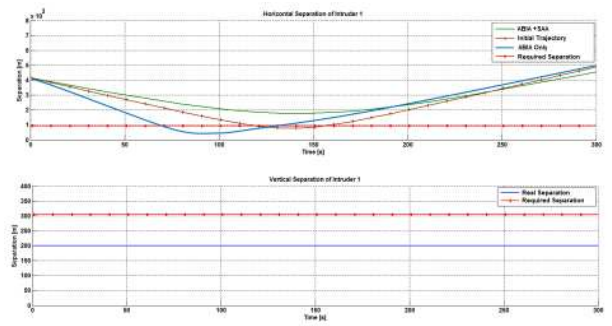


Fig. 28. Obtained horizontal and vertical separation of intruder 1.

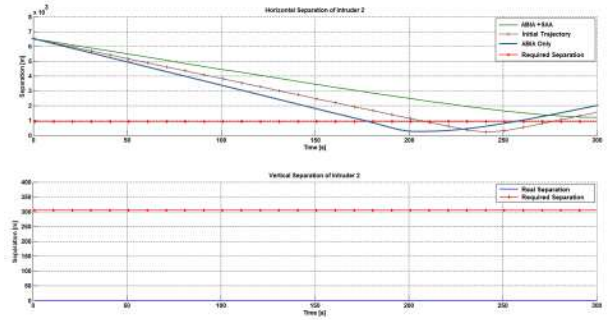


Fig. 29. Obtained horizontal and vertical separation of intruder 2.

The simulation results demonstrate that the ABIA IFG module is capable of generating integrity flags to provide both caution and warning signals when GNSS signals are degraded or lost. After the integrity caution flag is generated, the time available for the pilot/autopilot to react (before the integrity event is detected and the warning flag is generated), is at least 2 seconds. This TTC can support safety-critical tasks including GLS curved/segmented precision approach and automatic landing applications. Data analysis showed that the ABIA system can provide useful integrity signals for CAT-III precision approach and automatic landing (automated and real-time FPO is essential in this case). In the C-SAA and N-SAA scenarios investigated and in the dynamic conditions explored, all near mid-air collision threats were successfully avoided by implementing adequate trajectory optimisation algorithms. Both PSO and DGO algorithms proved successful in C-SAA and N-SAA scenarios depending on the available time for the optimisation loops (distance host-intruders and relative dynamics).

## 7. CONCLUSIONS AND FUTURE WORK

In this research the synergies between a GNSS Avionics Based Integrity Augmentation (ABIA) system and a novel Unmanned Aerial System (UAS) Sense-and-Avoid (SAA) architecture for cooperative and non-cooperative scenarios were explored. The integration of ABIA with SAA leads to an Integrity Augmented SAA (IAS) solution allowing safe and unrestricted access of UAS to commercial airspace. The ABIA and SAA research activities were presented and a detailed ABIA/SAA integrated architecture was established.

Simulation case studies were performed for IFG, IFG/FPM and ABIA/SAA modules. The trajectory optimization problem was mathematically formulated and the real-time capability of the FPOM (using pseudospectral and other methods) was verified. From the results of the simulation activity, the following conclusions can be drawn:

- The design of an Avionics Based Integrity Augmentation (ABIA) system for GNSS applications was accomplished.
- The ABIA Integrity Flag Generator (IFG) is capable of generating integrity flag to provide both caution (predictive) and warning signals to the pilot when GNSS signals are degraded or lost.
- According to the simulation results, after the integrity caution flag is generated, the time available for the pilot/autopilot to react (before the integrity warning flag is generated), is sufficient for safety-critical tasks including GLS curved/segmented precision approach and automatic landing applications.
- Data analysis shows that the ABIA system can provide the level of integrity required for CAT-III precision approach, which are not currently available with LAAS.
- The ABIA integration into an existing UAV SAA architecture proved that all near mid-air collision threats were successfully avoided by implementing trajectory optimisation algorithms.
- The proposed ABIA/SAA integration architecture is capable of achieving adequate performance by avoiding critical satellite signal losses while fulfilling the separation requirements for SAA set by international aviation organisations.

Further research is focussing on the following areas:

- Improve the aircraft flight dynamics model and complete the development of a Manoeuvre Identification Algorithm (MIA) suitable for incorporation in the ABIA flight path optimisation module.
- Examine other types of manned aircraft (e.g., civil airliners) and Unmanned Aerial Vehicles (UAVs), as well as unconventional body shapes (e.g., blended wings aircraft).
- Perform additional research on multipath detection and isolation in various kinds of receivers for avionics applications.

Additional long-term objectives of this research include the following:

- Investigate and compare different types of avionics sensor technologies and their potential to support the design of robust ABAS/ABIA architectures for manned A/C and UAVs.
- Extend the ABAS/ABIA concepts to the Aeronautical Data Link (ADL) application domain and investigate ABIA LOS and BLOS communications interfaces for UAS applications.

- Investigate ABIA evolution for Next Generation Flight Management System (NG-FMS) applications [38-41]:
  - Trajectory Optimization for Future CNS+A Systems.
  - 4DT Intent Based Operations.
  - NG-FMS/ABIA Integration.
- Study possible applications of the ABAS/ABIA concepts to advanced mission planning and forensic (accident investigation) applications.
- Evaluate the potential of ABAS/ABIA to enhance the performance of next generation CNS/ATM systems for Performance/Intent Based Operations (PBO/IBO) and Four-Dimensional Trajectory (4DT) management.

## REFERENCES

- [1] R. Sabatini, T. Moore and C. Hill, "A New Avionics Based GNSS Integrity Augmentation System: Part 1 – Fundamentals," *Journal of Navigation*, Vol. 66, No. 3, pp. 363-383, May 2013. DOI: 10.1017/S0373463313000027
- [2] R. Sabatini, T. Moore and C. Hill, "A New Avionics Based GNSS Integrity Augmentation System: Part 2 – Integrity Flags," *Journal of Navigation*, Vol. 66, No. 4, pp. 511-522, June 2013. DOI: 10.1017/S0373463313000143
- [3] R. Sabatini, T. Moore, C. Hill, "A Novel GNSS Integrity Augmentation System for Civil and Military Aircraft," *International Journal of Mechanical, Aerospace, Industrial and Mechatronics Engineering*, Vol. 7, No. 12, pp. 1433-1449, International Science Index, December 2013.
- [4] R. Sabatini, T. Moore and C. Hill. "A Novel Avionics-Based GNSS Integrity Augmentation System for UAV Applications," Paper presented at the Royal Institute of Navigation (RIN) Conference on Unmanned Air Vehicles - Sharing the Airspace, Teddington (UK), February 2013.
- [5] R. Sabatini, T. Moore and C. Hill. "Avionics Based GNSS Integrity Augmentation for Mission- and Safety-Critical Applications," Paper presented at 25<sup>th</sup> International Technical Meeting of the Satellite Division of the Institute of Navigation: ION GNSS-2012, Nashville (Tennessee), September 2012.
- [6] E.D. Kaplan and C.J. Hegarty, "Understanding GPS: Principles and Applications," Artech House, Second Edition, 2006.
- [7] RTCA DO-245A, "Minimum Aviation System Performance Standards for Local Area Augmentation System (LAAS)," Dec 2004.
- [8] O.M Mubarak and A.G Dempster, "Analysis of Early Late Phase in Single and Dual Frequency GPS Receivers for Multipath Detection," The University of New South Wales (Australia), 2010. Available at

- [http://www.gmat.unsw.edu.au/snap/staff/omer\\_mubarak.htm](http://www.gmat.unsw.edu.au/snap/staff/omer_mubarak.htm).
- [9] P. Ward, "Using a GPS Receiver Monte Carlo Simulator to Predict RF Interference Performance," Proceedings of 10<sup>th</sup> International Technical Meeting of The Satellite Division of The Institute of Navigation, Kansas City, MO, pp.1473–1482, September 1997.
- [10] P. Ward, "GPS Receiver RF Interference Monitoring, Mitigation, and Analysis Techniques," NAVIGATION, Journal of the Institute of Navigation, Vol. 41, No. 4 (Winter), pp. 367-391, 1994-95.
- [11] M.S. Braasch, "On the Characterization of Multipath Errors in Satellite-based Precision Approach and Landing Systems," College of Engineering and Technology, Ohio University, June 1992.
- [12] R. Sabatini and G. Palmerini, "Differential Global Positioning System (DGPS) for Flight Testing," NATO Research and Technology Organization (RTO) – Systems Concepts and Integration Panel (SCI), AGARDograph Series RTO-AG-160, Vol. 21, Oct 2008.
- [13] S.B. Hottman, K.R. Hansen and M. Berry, "Literature Review on Detect, Sense, and Avoid Technology for Unmanned Aircraft Systems," Tech. Report DOT/FAA/AR-08/41, US Department of Transport, USA, 2009.
- [14] A. Muraru, "A Critical Analysis of Sense and Avoid Technologies for Modern UAVs," Advances in Mechanical Engineering, ISSN: 2160-0619, Vol 2, No.1, March 2012. DOI:10.5729/ame.vol2.issue1.23
- [15] S. Ramasamy, R. Sabatini and A. Gardi, "Avionics Sensor Fusion for Small Size Unmanned Aircraft Sense-and-Avoid," Paper presented at IEEE Workshop on Metrology for Aerospace, pp. 271-276, Benevento (Italy), May 2014. DOI: 10.1109/MetroAeroSpace.2014.6865933
- [16] P. Rodriguez, R. Sabatini, A. Gardi and S. Ramasamy, "A Novel System for Non-Cooperative UAV Sense-and-Avoid," Paper presented at European Navigation Conference 2013, Vienna, Austria, April 2013.
- [17] M.J. Kochenderfer, L.P. Espindle, J.D. Griffith and J.K. Kuchar, "Encounter Modeling for Sense and Avoid Development," Paper presented at Integrated Communications, Navigation and Surveillance Conference (ICNS), pp. 1-10, 2008. DOI: 10.1109/ICNSURV.2008.4559177
- [18] Federal Aviation Administration, "Pilot's Role in Collision Avoidance," AC90-48C, Washington DC, USA, 1983.
- [19] C.G. Prévost, A. Desbiens, E. Ganon, and D. Hodouin, "UAV Optimal Obstacle Avoidance while Respecting Target Arrival Specifications," in Preprints of the 18<sup>th</sup> IFAC World Congress, Milano, Italy, pp. 11815-11820, 2008.
- [20] DOT/FAA/CT-96-1, "Human Factors Design Guide for Acquisition of Commercial-Off-The-Shelf Subsystems," Non-Developmental Items, and Developmental Systems-Final Report and Guide, January 1996.
- [21] P. Cornic, P. Garrec, S. Kemkemian, L. Ratton, "Sense and Avoid Radar using Data Fusion with Other Sensors," Paper presented at the IEEE Aerospace Conference, Big Sky, USA, March 2010. DOI: 10.1109/AERO.2011.5747514
- [22] J. Lai, J.J Ford, L. Mejias, P. O'Shea and R. Walker, "See and Avoid Using Onboard Computer Vision," Sense and Avoid in UAS Research and Applications, Plamen Angelov (ed.), John Wiley and Sons, West Sussex, UK, 2012.
- [23] R. Sabatini, "Airborne Laser Systems Performance Prediction, Safety Analysis, Flight Testing and Operational Training," PhD Thesis, School of Engineering, Cranfield University, UK, 2003.
- [24] R. Sabatini, S. Ramasamy, A. Gardi and L.R. Salazar, "Low-cost Sensors Data Fusion for Small Size Unmanned Aerial Vehicles Navigation and Guidance," International Journal of Unmanned Systems Engineering, Vol. 1, No. 3, pp. 16-47, August 2013.
- [25] R. Sabatini, C. Bartel, A. Kaharkar, T. Shaid and S. Ramasamy, "Navigation and Guidance System Architectures for Small Unmanned Aircraft Applications," International Journal of Mechanical, Aerospace, Industrial and Mechatronics Engineering, Vol. 8, No. 4, pp. 733-752, International Science Index, April 2014.
- [26] Z. Zhenjiang, Y. Meng, C. Hutao and C. Pingyuan, "The Method to Determine Spherical Harmonic Model of Asteroid based on Polyhedron," Paper presented at the 3<sup>rd</sup> International Conference on Computer and Electrical Engineering, International Proceedings of Computer Science and Information Technology, Vol. 53, 2012.
- [27] R. Sabatini, F. Cappello, S. Ramasamy, A. Gardi and R. Clothier, "An Innovative Navigation and Guidance System for Small Unmanned Aircraft using Low-Cost Sensors," In press, Aircraft Engineering and Aerospace Technology, Emerald Publishing Group Ltd., 2014.
- [28] R. Sabatini, A. Gardi and S. Ramasamy, "A Laser Obstacle Detection and Avoidance System for Unmanned Aircraft Sense-and-Avoid," Applied Mechanics and Materials, Vol. 629, Trans Tech Publications, Switzerland, pp. 355-360, 2014. DOI: 10.4028/www.scientific.net/AMM.629.355
- [29] R. Sabatini, A. Gardi and M. A. Richardson, "LIDAR Obstacle Warning and Avoidance System for Unmanned Aircraft," International Journal of Mechanical, Aerospace, Industrial and Mechatronics Engineering, Vol. 8, No. 4, pp. 62-73, International Science Index, April 2014.

- [30] YUMA GPS Almanacs. Available at: <http://www.celestrak.com/GPS/almanac/Yuma/definition.asp>.
- [31] SEM GPS Almanacs. Available at: <http://www.celestrak.com/GPS/almanac/SEM/definition.asp>.
- [32] Anonymous, "Aircraft Drawings". Available at <http://www.aircraftdrawingsdownload.com>.
- [33] M.T. Burston, R. Sabatini, R. Clothier, A. Gardi, and S. Ramasamy, "Reverse Engineering of a Fixed Wing Unmanned Aircraft 6-DoF Model for Navigation and Guidance Applications," Applied Mechanics and Materials, Vol. 629, Trans Tech Publications, Switzerland, pp. 164-169, 2014. DOI: 10.4028/www.scientific.net/AMM.629.164
- [34] R. Sabatini, M.A. Richardson, C. Bartel, A. Kaharkar, T. Shaid, L. Rodriguez and S. Ramasamy, "A Low-cost Vision Based Navigation System for Small Size Unmanned Aerial Vehicle Applications," Journal of Aeronautics and Aerospace Engineering, Vol. 2, No. 3, May 2013. DOI: 10.4172/2168-9792.1000110
- [35] R. Sabatini, A. Kaharkar, C. Bartel and T. Shaid, "Carrier-phase GNSS Attitude Determination and Control for Small UAV Applications," Journal of Aeronautics and Aerospace Engineering, Vol. 2, No. 4, July 2013. DOI: 10.4172/2168-9792.1000115
- [36] R. Sabatini, L. Rodríguez, A. Kaharkar, C. Bartel and T. Shaid, "Carrier-phase GNSS Attitude Determination and Control System for Unmanned Aerial Vehicle Applications," ARPN Journal of Systems and Software, ISSN: 2222-9833, Vol. 2, Issue 11, pp. 297-322. December 2012.
- [37] B.W. Parkinson and J.J. Spilker Jr., "Global Positioning System: Theory and Applications," Vol. I, AIAA - Progress in Astronautics and Aeronautics, 1996.
- [38] R. Sabatini, Y. Liu, K. De Ridder, A. Gardi, S. Ramasamy, D. Zammit-Mangion and L. Rodriguez, "ENDEAVOUR Project – Novel Avionics and ATM Systems for SESAR and NextGen," Paper presented at the Conference Avionics Europe 2013 – Tackling the Challenges in Avionics: Single Sky Many Platforms, Munich (Germany), February 2013.
- [39] S. Ramasamy, R. Sabatini, A. Gardi and T. Kistan, "Next Generation Flight Management System for Real-Time Trajectory Based Operations," Applied Mechanics and Materials, Vol. 629, Trans Tech Publications. Switzerland. Pp. 344-349. 2014. DOI: 10.4028/www.scientific.net/AMM.629.344
- [40] S. Ramasamy, M. Sangam, R. Sabatini and A. Gardi, "Flight Management System for Unmanned Reusable Space Vehicle Atmospheric and Re-entry Trajectory Optimisation," Applied Mechanics and Materials," Vol. 629, Trans Tech Publications, Switzerland, pp. 304-309. 2014. DOI: 10.4028/www.scientific.net/AMM.629.304
- [41] A. Gardi, R. Sabatini, S. Ramasamy and T. Kistan, "Real-Time Trajectory Optimisation Models for Next Generation Air Traffic Management Systems," Applied Mechanics and Materials, Vol. 629, Trans Tech Publications. Switzerland, pp. 327-332, 2014. DOI: 10.4028/www.scientific.net/AMM.629.327